Journal of Computational Physics 229 (2010) 5615–5629

Contents lists available at ScienceDirect

Journal of Computational Physics

journal homepage: www.elsevier.com/locate/jcp

Non-conformal domain decomposition method with second-order transmission conditions for time-harmonic electromagnetics

Zhen Peng *, Jin-Fa Lee

ElectroScience Laboratory, The Ohio State University, 1320 Kinnear Road, Columbus, OH 43212, USA

ARTICLE INFO

Article history:
Received 29 December 2009
Received in revised form 30 March 2010
Accepted 31 March 2010
Available online 10 April 2010

Keywords:
Domain decomposition methods
Second-order transmission conditions
Maxwell's equations

ABSTRACT

Non-overlapping domain decomposition (DD) methods provide efficient algorithms for solving time-harmonic Maxwell equations. It has been shown that the convergence of DD algorithms can be improved significantly by using high order transmission conditions. In this paper, we extend a newly developed second-order transmission condition (SOTC), which involves two second-order transverse derivatives, to facilitate fast convergence in the non-conformal DD algorithms. However, the non-conformal nature of the DD methods introduces an additional technical difficulty, which results in poor convergence in many real-life applications. To mitigate the difficulty, a corner-edge penalty method is proposed and implemented in conjunction with the SOTC to obtain truly robust solver performance. Numerical results verify the analysis and demonstrate the effectiveness of the proposed methods on a few model problems. Finally, drastically improved convergence, compared to the conventional Robin transmission condition, was observed for an electrically large problem of practical interest.

1. Introduction

Non-overlapping domain decomposition (DD) methods have recently attracted considerable attention due to their ability to accurately and efficiently solve large and multi-scale electromagnetic radiation and scattering problems [2–12]. It is well known that the convergence of the DD algorithms depends strongly upon the nature of the transmission conditions that communicate information between adjacent sub-domains [6,13–15]. Després showed [2] that the use of a complex Robin TC would lead to the iterative process converging quickly for propagating eigenmodes, though the evanescent modes are non-convergent. The optimized TCs of Dolean et al. [3], by including a single second-order transverse derivative, allow the convergence of both sets of modes. However, in order to obtain convergence of evanescent modes, the optimized TCs must trade in some performance of the propagating modes. Thus, the optimized TCs do not always provide better convergence against the conventional Robin TC. In [6], a new type of SOTC, called SOTC-TE, which is shown to shift eigenvalues that correspond to transverse electric (TE) evanescent modes away from zero. While the DD method with SOTC-TE significantly improves the convergence w.r.t. the 1st order Robin TC, it is only effective in preconditioning one set of problematic eigenmodes. The eigenmodes neglected by the SOTC-TE, namely the transverse magnetic (TM) evanescent modes, present the last impediment to solver convergence. We address these modes by introducing a full second-order TC (SOTC-Full) that includes an additional term with a second-order transverse derivative.

The SOTC-Full was first proposed and implemented in Ref. [5] for improving matrix convergences in conformal DD methods. However, the incorporation of the SOTC-Full in the finite element implementation of conformal DD methods

* Corresponding author. Tel.: +1 614 302 8896.
E-mail addresses: peng.98@osu.edu (Z. Peng), lee.1863@osu.edu (J.-F. Lee).

0021-9991/$ - see front matter © 2010 Elsevier Inc. All rights reserved.
doi:10.1016/j.jcp.2010.03.049

[5] results in a singular system matrix. This is due to the fact that the auxiliary variables, **j**, which represent the electric currents on the interfaces, were defined discontinuously over the interfaces. This gives rise to redundant basis functions on edges shared by two or more interfaces. Nonetheless, in the conformal DD methods, the excitation is kept in the range of the system matrix, and consequently the singular eigenvalues have little or no impact on the convergence. But, the scenarios are different once we extend the application of the SOTC-Full to the non-conformal DD methods. In the presence of non-conformal meshes, or non-matching triangulations, the original zero eigenvalues become small eigenvalues near zero. The occurrence of these small eigenvalues greatly affects negatively the convergence of the non-conformal DD methods, as will be shown later. In this paper, we propose a corner-edge penalty method to remove the problematic singular eigenvalues in the conformal and the small eigenvalues of the non-conformal DD methods, respectively. Numerical results verify the analysis and demonstrate the effectiveness of the proposed corner-edge penalty method.

The rest of the paper is organized as follows: In Section 2.1 we introduce the non-overlapping domain decomposition scheme and a full second-order TC. The FEM implementation is shortly discussed and reviewed in Section 2.2, followed by a study of the effect of the small eigenvalues on non-conformal DD methods. Subsequently, a corner-edge penalty method is proposed and demonstrated analytically through the eigen-spectrum of the resulting matrix. In Section 3 we illustrate the performance of non-conformal DD with SOTC-Full on a model waveguide example, a microstrip photonic-bandgap structure (PBG) and a microwave photonic crystal structure. A summary and conclusion are included in Section 4.

2. Formulation

2.1. Domain decomposition with second-order transmission condition

A detailed explanation on the notations used in this section can be found in Ref. [1,6]. We begin by defining a boundary value problem (BVP) for the decomposed problem of Fig. 1. It can be written as

$$\nabla \times \mu_{ri}^{-1} \nabla \times \mathbf{E}_i - k_0^2 \varepsilon_{ri} \mathbf{E}_i = -jk_0 \eta_0 \mathbf{J}_i^{imp} \quad \text{in } \Omega_i \tag{1}$$

$$\nabla \times \mu_{rj}^{-1} \nabla \times \mathbf{E}_j - k_0^2 \varepsilon_{rj} \mathbf{E}_j = -jk_0 \eta_0 \mathbf{J}_j^{imp} \quad \text{in } \Omega_j \tag{2}$$

$$\pi_\tau(\mathbf{E}_i) = \pi_\tau(\mathbf{E}_j) \quad \text{on } \Gamma \tag{3}$$

$$\gamma_\tau(\mu_{ri}^{-1} \nabla \times \mathbf{E}_i) = \gamma_\tau(\mu_{rj}^{-1} \nabla \times \mathbf{E}_j) \quad \text{on } \Gamma \tag{4}$$

$\forall i, j \in \{1,2,3,4\}$ and $\mathbf{E}_i \in \mathbf{H}_0(\text{curl}; \Omega_i)$ and $\mathbf{E}_j \in \mathbf{H}_0(\text{curl}; \Omega_j)$ represent the electric fields in two adjacent sub-domains. Moreover, $\pi_\tau(\cdot)$ and $\gamma_\tau(\cdot)$ are the surface tangential trace, $\hat{\mathbf{n}} \times \cdot \times \hat{\mathbf{n}}$, and the surface twist tangential trace, $\hat{\mathbf{n}} \times \cdot$, respectively. In what follows, we abuse the notation somewhat and split Γ into Γ_{ij}, the interface as seen from Ω_i, and Γ_{ji}, the interface as seen from Ω_j. We do so to emphasize the fact that the interface meshes on Γ_{ij} and Γ_{ji} are allowed to be non-conformal. Eqs. (3) and (4) enforce the tangential continuities of the electric and magnetic fields of the otherwise unconstrained sub-domain fields. These conditions render the decomposed BVP above equivalent to the original problem in the entire domain Ω. We ignore the exterior boundary and other boundary conditions as they can be accounted for in much the same way as in conventional finite element discretizations.

In what follows, we replace the interface conditions, (3) and (4), with the newly developed full second-order transmission condition (SOTC-Full), see [5]. The SOTC-Full, which includes two second-order transverse derivatives, can be expressed as

$$\begin{aligned} &\gamma_\tau(\mu_{ri}^{-1} \nabla \times \mathbf{E}_i) + \alpha \pi_\tau(\mathbf{E}_i) + \beta \nabla_\tau \times \nabla_\tau \times \pi_\tau(\mathbf{E}_i) + \gamma \nabla_\tau \nabla_\tau \cdot \gamma_\tau(\mu_{ri}^{-1} \nabla \times \mathbf{E}_i) \\ &\quad = -\gamma_\tau(\mu_{rj}^{-1} \nabla \times \mathbf{E}_j) + \alpha \pi_\tau(\mathbf{E}_j) + \beta \nabla_\tau \times \nabla_\tau \times \pi_\tau(\mathbf{E}_j) - \gamma \nabla_\tau \nabla_\tau \cdot \gamma_\tau(\mu_{rj}^{-1} \nabla \times \mathbf{E}_j) \end{aligned} \tag{5}$$

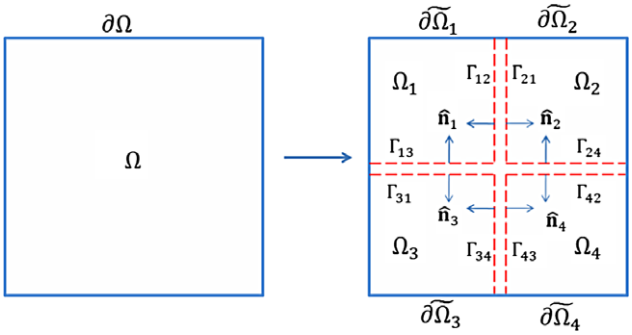

Fig. 1. Notations for decomposition of the domain.

$$\gamma_\tau(\mu_{rj}^{-1}\nabla\times\mathbf{E}_j)+\alpha\pi_\tau(\mathbf{E}_j)+\beta\nabla_\tau\times\nabla_\tau\times\pi_\tau(\mathbf{E}_j)+\gamma\nabla_\tau\nabla_\tau\cdot\gamma_\tau(\mu_{rj}^{-1}\nabla\times\mathbf{E}_j)$$
$$=-\gamma_\tau(\mu_{ri}^{-1}\nabla\times\mathbf{E}_i)+\alpha\pi_\tau(\mathbf{E}_i)+\beta\nabla_\tau\times\nabla_\tau\times\pi_\tau(\mathbf{E}_i)-\gamma\nabla_\tau\nabla_\tau\cdot\gamma_\tau(\mu_{ri}^{-1}\nabla\times\mathbf{E}_i) \quad (6)$$

with complex coefficients α, β and γ to be determined. It is shown in Appendix A that if ($\Im(\frac{\beta}{\alpha})\neq 0$ or $\Re(\frac{\beta}{\alpha})\geqslant 0$) and ($\Im(\gamma)\neq 0$ or $\Re(\gamma)\leqslant 0$) the above transmission conditions, Eqs. (5) and (6), enforce the necessary continuities of the electric and magnetic fields on the interface between sub-domains.

Similar to [6], we can assess the convergence behavior of the DD algorithm, which uses the SOTC-Full. There, we employ an idealized decomposition of $\mathbb{R}^3$ with Γ defined to be the plane $z=0$, $\Omega_1=\mathbb{R}^2\times(\infty,0]$, and $\Omega_2=\mathbb{R}^2\times[0,\infty)$. To further simplify the analysis, we consider plane waves in free space traveling in the yz-plane with dispersion relation $k^2=k_y^2+k_z^2$. Here k_z denotes the $\hat{z}$-directed wave number and k_y denotes the $\hat{y}$-directed wave number as well. A real, positive k_z is said to be propagating mode while imaginary k_z refers to evanescent mode. The TC is imposed on Γ and an iterative solution process is considered. The convergence factors of the iterative algorithm are determined as functions k_z using a decomposition of the solution into transverse electric (TE) and transverse magnetic (TM) components. The magnitude of the convergence factor corresponds to spectral radius (the maximum magnitude of the eigenvalues) of the DD algorithm operator. An operator with a spectral radius $\rho<1$ is said to be convergent because a simple stationary iterative algorithm is guaranteed to converge to the solution.

With this SOTC-Full, the convergence factor of TE modes is the same as the SOTC-TE in [6]. Namely, we obtain

$$|\rho_{\mathrm{TE}}|=\left|\frac{jk_z+\alpha+\beta(k^2-k_z^2)}{jk_z-\alpha-\beta(k^2-k_z^2)}\right|^2 \quad (7)$$

The proper choice of β provide convergence of the TE evanescent modes. We set that $\alpha=jk$ and $\beta=\frac{j}{k+\tilde{k}_z^{\mathrm{TE}}}$ to obtain the convergence factors given by

$$|\rho_{\mathrm{TE}}|=\left|\frac{(k-k_z)(\tilde{k}_z^{\mathrm{TE}}-k_z)}{(k+k_z)(\tilde{k}_z^{\mathrm{TE}}+k_z)}\right|^2 \quad (8)$$

We are free to choose an additional zero (the first zero occur at $k=k_z$) to occur for an evanescent mode by choosing an imaginary $\tilde{k}_z^{\mathrm{TE}}$ and thereby provide convergence of the TE evanescent modes.

In addition to the terms of the SOTC-TE, we have now included a $\nabla_\tau\nabla_\tau\cdot$ term. The inclusion of this additional term is motivated by the approximation to the TM transparent condition, the exact relation satisfied by a TM-polarized plane wave incident upon an infinite plane. Thereby, the convergence factor of TM evanescent modes is obtained as

$$|\rho_{\mathrm{TM}}|=\left|\frac{-j\alpha k_z+k^2-\gamma k^2(k^2-k_z^2)}{j\alpha k_z+k^2-\gamma k^2(k^2-k_z^2)}\right|^2 \quad (9)$$

Analogously to the TE evanescent case, we may now choose γ such that TM evanescent modes converge. By selecting $\gamma=\frac{1}{k^2+k\tilde{k}_z^{\mathrm{TM}}}$, we write

$$|\rho_{\mathrm{TM}}|=\left|\frac{(k-k_z)(\tilde{k}_z^{\mathrm{TM}}-k_z)}{(k+k_z)(\tilde{k}_z^{\mathrm{TM}}+k_z)}\right|^2 \quad (10)$$

We see that an additional zero of the convergence factor can be chosen for a TM evanescent mode. Here, we have chosen $\tilde{k}_z^{\mathrm{TE}}=-j\sqrt{(k_\tau^{\max,\mathrm{TE}})^2-k^2}$ and $\tilde{k}_z^{\mathrm{TM}}=-j\sqrt{(k_\tau^{\max,\mathrm{TM}})^2-k^2}$. Moreover, $k_\tau^{\max,\mathrm{TE}}$ and $k_\tau^{\max,\mathrm{TM}}$ denote the chosen maximum transverse wave number supported on the interfaces for TE and TM modes, respectively. This depends upon both mesh size and the polynomial order of the field expansion. As the mesh size, h, decreases, the maximum supported wave number increases at a rate proportional to π/h. In addition, we assume a linear dependence on the order p of the polynomial representation. Thus we write that $k_\tau^{\max,\mathrm{TE}}=c_{\mathrm{TE}}(\frac{\pi p}{h})$ and $k_\tau^{\max,\mathrm{TM}}=c_{\mathrm{TM}}(\frac{\pi p}{h})$. Note that we use different constants c_{TE} and c_{TM} to account for the fact that, the TE field is represented with greater accuracy than that of the magnetic field obtain from $\nabla\times\mathbf{E}$. Fig. 2 illustrates the convergence factors where we have set $k_\tau^{\max,\mathrm{TE}}=3k$ and $k_\tau^{\max,\mathrm{TM}}=2k$ as an example.

2.2. FEM implementation

Herein, the FEM implementation of the SOTC-Full in the non-conformal DDM algorithm is slightly different from [6]. We first introduce auxiliary variables $\mathbf{j}_i\in\mathbf{H}(\mathrm{curl}_\Gamma,\Gamma_{ij})$ and $\mathbf{j}_j\in\mathbf{H}(\mathrm{curl}_\Gamma,\Gamma_{ji})$ representing the electric currents on the two sides of the interface:

$$\mathbf{j}_i=\frac{1}{k_0}\gamma_\tau(\mu_{ri}^{-1}\nabla\times\mathbf{E}_i) \quad (11)$$

$$\mathbf{j}_j=\frac{1}{k_0}\gamma_\tau(\mu_{rj}^{-1}\nabla\times\mathbf{E}_j) \quad (12)$$

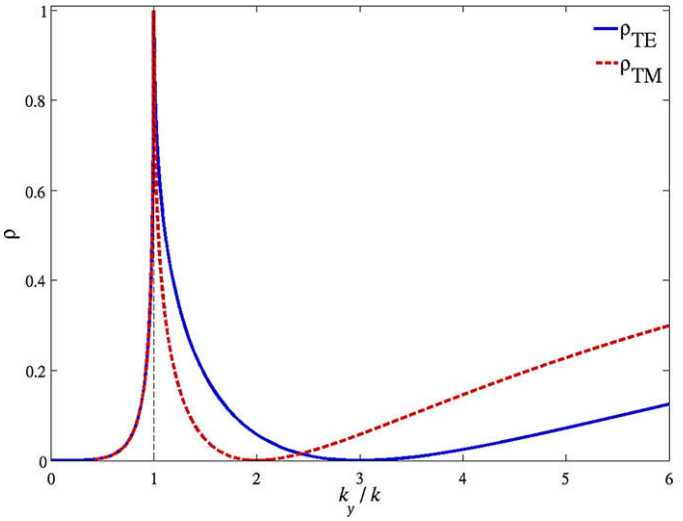

Fig. 2. Convergence factor of SOTC-Full.

Additionally, in order to implement the $\nabla_\tau\nabla_\tau\cdot$ term, we need to introduce an additional scalar (charge) variable $\rho_i \in H_0^{-1/2}(\Gamma_{ij})$ and $\rho_j \in H_0^{-1/2}(\Gamma_{ji})$

$$\rho_i = \frac{1}{k_0}\nabla_\tau\cdot\mathbf{j}_i = \frac{1}{k_0^2}\nabla_\tau\cdot\gamma_\tau(\mu_{ri}^{-1}\nabla\times\mathbf{E}_i) \tag{13}$$

$$\rho_j = \frac{1}{k_0}\nabla_\tau\cdot\mathbf{j}_j = \frac{1}{k_0^2}\nabla_\tau\cdot\gamma_\tau(\mu_{rj}^{-1}\nabla\times\mathbf{E}_j) \tag{14}$$

Furthermore, we define $\mathbf{e}_i = \pi_\tau(\mathbf{E}_i)$ and $\mathbf{e}_j = \pi_\tau(\mathbf{E}_j)$ for convenience. With the introductions of these auxiliary variables, the TCs in (5) and (6) can be rewritten as

$$k_0\mathbf{j}_i + \alpha_i\mathbf{e}_i + \beta\nabla_\tau\times\nabla_\tau\times\mathbf{e}_i + \gamma k_0^2\nabla_\tau\rho_i = -k_0\mathbf{j}_j + \alpha_i\mathbf{e}_j + \beta\nabla_\tau\times\nabla_\tau\times\mathbf{e}_j - \gamma k_0^2\nabla_\tau\rho_j \tag{15}$$

$$k_0\mathbf{j}_j + \alpha_j\mathbf{e}_j + \beta\nabla_\tau\times\nabla_\tau\times\mathbf{e}_j + \gamma k_0^2\nabla_\tau\rho_j = -k_0\mathbf{j}_i + \alpha_j\mathbf{e}_i + \beta\nabla_\tau\times\nabla_\tau\times\mathbf{e}_i - \gamma k_0^2\nabla_\tau\rho_i \tag{16}$$

with $\alpha_m = -jk_m = -jk_0\sqrt{\mu_{rm}\varepsilon_{rm}}$ to account for different materials across sub-domain interfaces.

Subsequently, these two TCs are tested with $\mathbf{u}_i \in \mathbf{H}(\mathrm{curl}_\Gamma, \Gamma_{ij})$ and $\mathbf{u}_j \in \mathbf{H}(\mathrm{curl}_\Gamma, \Gamma_{ji})$, and after performing an integration by parts, we have

$$\begin{aligned} &k_0\langle\mathbf{u}_i,\mathbf{j}_i\rangle_{\Gamma_{ij}} + \alpha_i\langle\mathbf{u}_i,\mathbf{e}_i\rangle_{\Gamma_{ij}} + \beta\langle\nabla_\tau\times\mathbf{u}_i,\nabla_\tau\times\mathbf{e}_i\rangle_{\Gamma_{ij}} + \gamma k_0^2\langle\mathbf{u}_i,\nabla_\tau\rho_i\rangle_{\Gamma_{ij}} \\ &\quad = -k_0\langle\mathbf{u}_i,\mathbf{j}_j\rangle_{\Gamma_{ij}} + \alpha_i\langle\mathbf{u}_i,\mathbf{e}_j\rangle_{\Gamma_{ij}} + \beta\langle\nabla_\tau\times\mathbf{u}_i,\nabla_\tau\times\mathbf{e}_j\rangle_{\Gamma_{ij}} - \gamma k_0^2\langle\mathbf{u}_i,\nabla_\tau\rho_j\rangle_{\Gamma_{ij}} \end{aligned} \tag{17}$$

$$\begin{aligned} &k_0\langle\mathbf{u}_j,\mathbf{j}_j\rangle_{\Gamma_{ji}} + \alpha_j\langle\mathbf{u}_j,\mathbf{e}_j\rangle_{\Gamma_{ji}} + \beta\langle\nabla_\tau\times\mathbf{u}_j,\nabla_\tau\times\mathbf{e}_j\rangle_{\Gamma_{ji}} + \gamma k_0^2\langle\mathbf{u}_j,\nabla_\tau\rho_j\rangle_{\Gamma_{ji}} \\ &\quad = -k_0\langle\mathbf{u}_j,\mathbf{j}_i\rangle_{\Gamma_{ji}} + \alpha_i\langle\mathbf{u}_j,\mathbf{e}_i\rangle_{\Gamma_{ji}} + \beta\langle\nabla_\tau\times\mathbf{u}_j,\nabla_\tau\times\mathbf{e}_i\rangle_{\Gamma_{ji}} - \gamma k_0^2\langle\mathbf{u}_j,\nabla_\tau\rho_i\rangle_{\Gamma_{ji}} \end{aligned} \tag{18}$$

The integration by parts on the $\nabla_\tau\times\nabla_\tau\times$ operator is somewhat suspect due to the discontinuity of the testing functions. However, we consider this to be a valid operation when the testing is rewritten as

$$\langle\mathbf{u}_i,\nabla_\tau\times\nabla_\tau\times(\mathbf{e}_i-\mathbf{e}_j)\rangle_{\Gamma_{ij}} = \langle\nabla_\tau\times\mathbf{u}_i,\nabla_\tau\times(\mathbf{e}_i-\mathbf{e}_j)\rangle_{\Gamma_{ij}} \tag{19}$$

and by noting that $\hat{\mathbf{n}}\times[\nabla\times(\mathbf{e}_i-\mathbf{e}_j)]$ goes to zero on the boundary of Γ_{ij} as a desired natural boundary condition.

Lastly, $\phi_i \in H_0^{-1/2}(\Gamma_{ij})$ and $\phi_j \in H_0^{-1/2}(\Gamma_{ji})$ are used to test the definition of the scalar auxiliary variable giving (after again an integration by parts)

$$k_0\langle\phi_i,\rho_i\rangle_{\Gamma_{ij}} + \langle\nabla_\tau\phi_i,\mathbf{j}_i\rangle_{\Gamma_{ij}} = 0 \tag{20}$$

$$k_0\langle\phi_j,\rho_j\rangle_{\Gamma_{ji}} + \langle\nabla_\tau\phi_j,\mathbf{j}_j\rangle_{\Gamma_{ji}} = 0 \tag{21}$$

We now introduce independent tetrahedral mesh, K_i, in each region Ω_i. The surface mesh induced on Γ_{ij} is denoted by $\mathcal{T}_{ij}$. On each of the sub-domain, we define discrete trial and test functions, $\mathbf{E}_i^h \in \mathbf{X}_i^h \subset \mathbf{H}_0(\mathrm{curl};\Omega_i)$ and $\mathbf{w}_i^h \in \mathbf{X}_i^h \subset \mathbf{H}_0(\mathrm{curl};\Omega_i)$, respectively. Here, $\mathbf{X}_i^h$ is taken to be the space of mixed order Nedelec basis functions defined in [16], with order $p = 2$. On

the interfaces, we introduce the discrete trial and test functions, $\rho_i^h \in Z_i^h$ and $\phi_i^h \in Z_i^h$ respectively, with $Z_i^h \subset H_0^{-1/2}(\Gamma_{ij})$. Z_i^h is taken to be the space interpolatory scalar basis functions with order $p = 2$. We also define discrete trial and test functions, $\mathbf{j}_i^h \in \mathbf{Y}_i^h$ and $\mathbf{u}_i^h \in \mathbf{Y}_i^h$ respectively, with $\mathbf{Y}_i^h \subset \mathbf{H}(\mathrm{curl}_\Gamma, \Gamma_{ij})$. $\mathbf{Y}_i^h$ will be taken as the two-dimensional restriction of $\mathbf{X}_i^h$, but with DOFs defined independently for each interface. Take the domain partition in Fig. 1 as an example. There are four domains meet at one set of corner edges. The auxiliary variables, $\mathbf{j}$, on these corner edges were defined discontinuously within the sub-domain. This gives rise to the redundant basis functions on these corner edges, and result in a singular DD matrix. For the conformal DD method described in [5], the excitations are kept in the ranges of the system matrices. These singular eigenvalues have little or no impact on the iterative solver convergence. However, for non-conformal DD method, these eigenvalues became very close to zero but not exactly zero and subsequently the convergence will deteriorate significantly. To successfully implement and enjoy the full benefits of the SOTC-Full for non-conformal DD methods, we will have to suppress these singular eigenvalues in the formulation.

2.3. Corner-edge penalty

In this section, we first examine the eigenvalue distributions that result from the DD matrices with discontinuous $\mathbf{j}_i$ variables on these corner edges. Then, we consider their behaviors w.r.t. both the conformal and non-conformal meshes. To do so, we use a $0.5\lambda_0 \times \lambda_0 \times \lambda_0$ air box with exterior boundaries terminated by a first order ABC. Here λ_0 is the wavelength in free space. The air box is partitioned into four equally sized sub-domains. These four sub-domains meet at one set of corner edges. Figs. 3 and 4 show the domain partitions and corner edges for conformal and non-conformal meshes, respectively.

The eigenspectra of the DD matrices using FOTC (First Order Transmission Condition) and SOTC-Full are shown in Figs. 5 and 6 for conformal (Fig. 3) and non-conformal (Fig. 4) meshes, respectively. By comparing eigenspectra of FOTC and SOTC-Full, we observe that most of the eigenvalues, in Figs. 5(a) and 6(a), that are on or very close to the shifted-unit-circle have

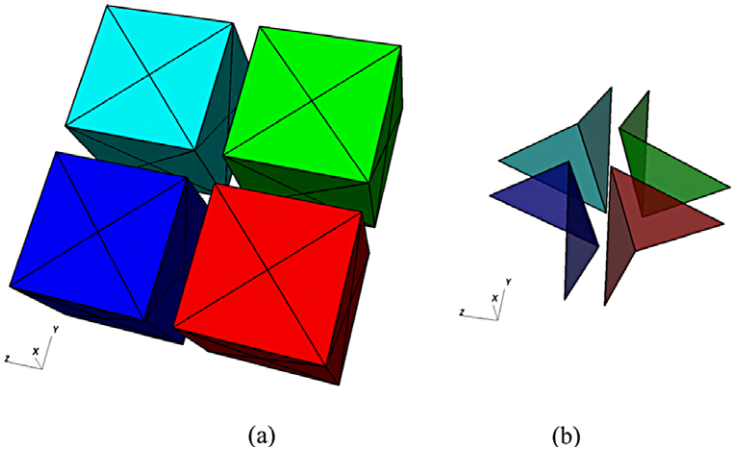

Fig. 3. DD with conformal meshes (a) domain partition; (b) corner edges.

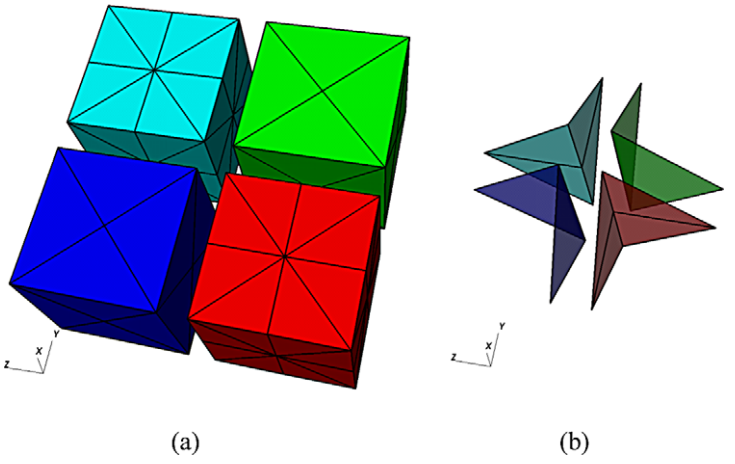

Fig. 4. DD with non-conformal meshes (a) domain partition; (b) corner edges.

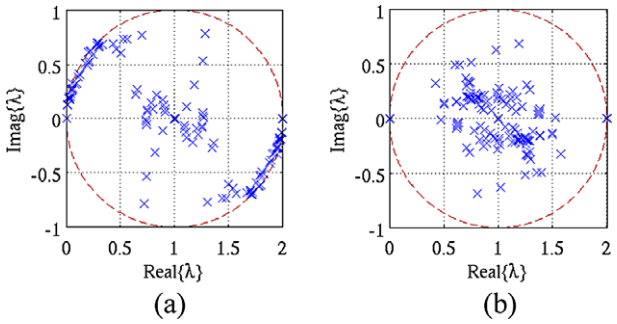

Fig. 5. Eigenspectra of conformal DD for an air box (a) DD with FOTC; (b) DD with SOTC-Full.

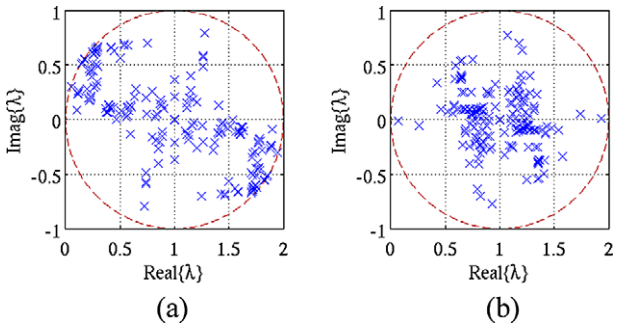

Fig. 6. Eigenspectra of non-conformal DD for an air box (a) DD with FOTC; (b) DD with SOTC-Full.

moved inside it in Figs. 5(b) and 6(b). These are evanescent modes affected by the SOTC-Full. We also see two interesting clusters in the figure, one is at 0 and the other at 2. These are caused by the redundancy of the **j** variables defined on the corner edges. The cluster of eigenvalues close to zero is of great concern. It indicates that the DD matrix to be solved is either singular or nearly singular. For conformal meshes, these clusters of eigenvalues are exactly at zero. These singular eigenvalues have little or no impact on the iterative solver convergence as the excitation is kept in the range of the system matrix. However, we note that for non-conformal meshes, these eigenvalues became very close to zero. These very small but non-zero eigenvalues are the ones that significantly degrade the performance of DD method. To verify this analysis, we use the same air box and partitions with mesh size $h = \lambda_0/8$ to study the performance of DD method. Fig. 7 shows the iterative solver convergence for conformal and non-conformal DD methods, using stopping-criteria of 10^{-8}. From Fig. 7, we witness that these eigenmodes have little if any impact on the convergence of the conformal DD method, but severely jeopardize the performance of the non-conformal DD method.

The above analysis shows that to obtain truly robust solver convergence of non-conformal DD methods with SOTC-Full, we need to address these singular eigenmodes. We accomplish this by considering the divergence free condition $\nabla\cdot\mathbf{B} = 0$, where **B** is the magnetic flux density. Fig. 8(a) shows the number of variables defined on the corner edges for DD partition with conformal mesh as shown in Fig. 3. Note that they are defined discontinuously over the interfaces. Assume a virtual cylinder, which encloses the set of corner edges shown in Fig. 8(b), the divergence free condition can be written as a surface integral over the cylinder $\int \mathbf{B}\cdot d\mathbf{S} = 0$.

Taking the limit of **d** goes to zero, the divergence free condition can be approximated by

$$\sum_N \int_C \mu_r s_N \frac{\theta_i}{2\pi}\mathbf{H}_N\cdot(\hat{\mathbf{n}}_N\times\hat{\mathbf{t}})dl = 0 \quad \forall N\in\{1,2,\ldots,8\};\ \forall i\in\{1,2,3,4\} \tag{22}$$

where $\mathbf{H}_N$ is the magnetic field on the corner edges, $\hat{\mathbf{n}}_N$ is the normal of the interface as indicated in Fig. 8(a), θ_i is the angle associated with each domain Ω_i, and $\hat{\mathbf{t}}$ is the direction along the corner edge C. The sign function, s_N, will be set to -1 and 1 for odd and even numbered corner edges, respectively. Considering the scenario $\theta_i = \frac{\pi}{2}, \forall i\in\{1,2,3,4\}$, straightforward manipulation shows that Eq. (22) is equivalent to

$$\sum_N \int_C \mu_r s_N(\mathbf{j}_N\cdot\hat{\mathbf{t}})dl = 0 \tag{23}$$

We then check whether the eigenvectors associated with the zero eigenvalues satisfy Eq. (23). In order to satisfy the divergence free condition, the entries in eigenvectors that corresponds to **j** variables on the corner edges should satisfy the following equation (assuming that $\mu_r = 1$ around the corner edge):

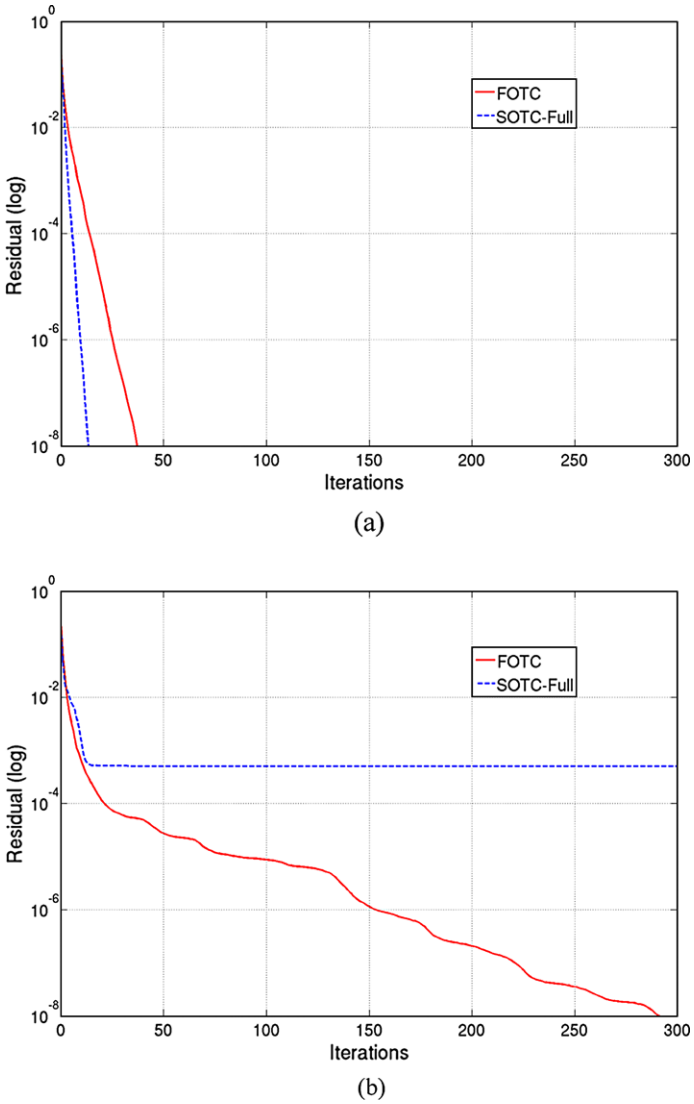

Fig. 7. Iterative solver convergence of DD method for an air box (a) conformal mesh; (b) non-conformal mesh.

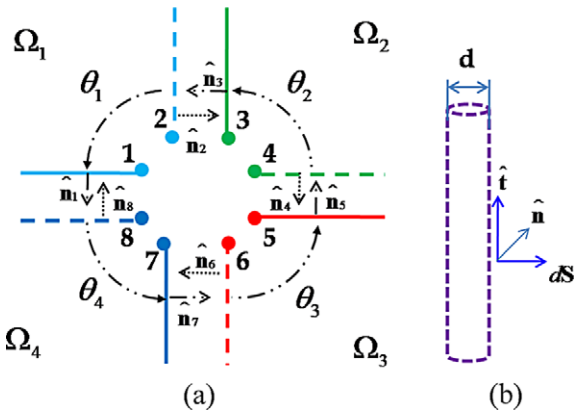

Fig. 8. Corners edges in Fig. 3(b), (a) numbering of the corner edges (front view); (b) virtual cylinder enclose the set of corner edges (side view).

$$-j_1 - j_3 - j_5 - j_7 + j_2 + j_4 + j_6 + j_8 = 0 \tag{24}$$

Tables 1a and 1b present the **j** corner edge entries in eigenvectors associated with zero and non-zero eigenvalues on these corner edges, respectively. From Table 1, it is evident that Eq. (24) is not satisfied for the eigenvectors corresponding to zero eigenvalues.

Once we recognized the nature of the eigenvectors that correspond to the zero eigenvalues in the conformal DD methods, we shall impose the needed constraint equations on the auxiliary variables, **j**, on all the corner edges. To do so, we define a line sesquilinear form as

$$\langle \mathbf{u}, \mathbf{v} \rangle_C = \int_C (\mathbf{u} \cdot \hat{\mathbf{t}}) \cdot (\mathbf{v} \cdot \hat{\mathbf{t}}) dl \tag{25}$$

For each set of corner edges, we now test Eq. (23) with $\mathbf{w}_i \in \mathbf{H}_0(\mathrm{curl}; \Omega_i)$, where Ω_i denote the sub-domain, which share this set of corner edges

$$\sum_N \left\langle \mathbf{w}_i, s_N \frac{\theta_i}{2\pi} \mathbf{j}_N \right\rangle_C = 0 \tag{26}$$

The final weak form of the DD method with full second-order TC is then given by:
Seek $(\mathbf{E}_i^h, \mathbf{E}_j^h) \in \mathbf{X}_i^h \times \mathbf{X}_j^h$, $(\mathbf{j}_i^h, \mathbf{j}_j^h) \in \mathbf{Y}_i^h \times \mathbf{Y}_j^h$, and $(\rho_i^h, \rho_j^h) \in Z_i^h \times Z_j^h$ such that

$$(\nabla \times \mathbf{w}_i^h, \mu_{ri}^{-1} \nabla \times \mathbf{E}_i^h)_{K_i} - k_0^2 (\mathbf{w}_i^h, \varepsilon_{ri} \mathbf{E}_i^h)_{K_i} + k_0 \langle \mathbf{w}_i^h, \mathbf{j}_i^h \rangle_{\Gamma_{ij}} = -jk_0 \eta_0 (\mathbf{w}_i^h, \mathbf{J}_i^{imp})_{K_i} \tag{27}$$

$$(\nabla \times \mathbf{w}_j^h, \mu_{rj}^{-1} \nabla \times \mathbf{E}_j^h)_{K_j} - k_0^2 (\mathbf{w}_j^h, \varepsilon_{rj} \mathbf{E}_j^h)_{K_j} + k_0 \langle \mathbf{w}_j^h, \mathbf{j}_j^h \rangle_{\Gamma_{ji}} = -jk_0 \eta_0 (\mathbf{w}_j^h, \mathbf{J}_j^{imp})_{K_j} \tag{28}$$

$$\begin{aligned} &k_0^2 \left\langle \mathbf{u}_i^h, \frac{1}{\alpha_i} \mathbf{j}_i^h \right\rangle_{\mathcal{T}_{ij}} + k_0 \langle \mathbf{u}_i^h, \mathbf{e}_i^h \rangle_{\mathcal{T}_{ij}} + k_0 \left\langle \nabla_\tau \times \mathbf{u}_i^h, \frac{\beta}{\alpha_i} \nabla_\tau \times \mathbf{e}_i^h \right\rangle_{\mathcal{T}_{ij}} + k_0^3 \left\langle \mathbf{u}_i^h, \frac{\gamma}{\alpha_i} \nabla_\tau \rho_i^h \right\rangle_{\mathcal{T}_{ij}} \\ &\quad = -k_0^2 \left\langle \mathbf{u}_i^h, \frac{1}{\alpha_i} \mathbf{j}_j^h \right\rangle_{\mathcal{T}_{ij}} + k_0 \langle \mathbf{u}_i^h, \mathbf{e}_j^h \rangle_{\mathcal{T}_{ij}} + k_0 \left\langle \nabla_\tau \times \mathbf{u}_i^h, \frac{\beta}{\alpha_i} \nabla_\tau \times \mathbf{e}_j^h \right\rangle_{\mathcal{T}_{ij}} - k_0^3 \left\langle \mathbf{u}_i^h, \frac{\gamma}{\alpha_i} \nabla_\tau \rho_j^h \right\rangle_{\mathcal{T}_{ij}} \end{aligned} \tag{29}$$

$$\begin{aligned} &k_0^2 \left\langle \mathbf{u}_j^h, \frac{1}{\alpha_j} \mathbf{j}_j^h \right\rangle_{\mathcal{T}_{ji}} + k_0 \langle \mathbf{u}_j^h, \mathbf{e}_j^h \rangle_{\mathcal{T}_{ji}} + k_0 \left\langle \nabla_\tau \times \mathbf{u}_j^h, \frac{\beta}{\alpha_j} \nabla_\tau \times \mathbf{e}_j^h \right\rangle_{\mathcal{T}_{ji}} + k_0^3 \left\langle \mathbf{u}_j^h, \frac{\gamma}{\alpha_j} \nabla_\tau \rho_j^h \right\rangle_{\mathcal{T}_{ji}} \\ &\quad = -k_0^2 \left\langle \mathbf{u}_j^h, \frac{1}{\alpha_j} \mathbf{j}_i^h \right\rangle_{\mathcal{T}_{ji}} + k_0 \langle \mathbf{u}_j^h, \mathbf{e}_i^h \rangle_{\mathcal{T}_{ji}} + k_0 \left\langle \nabla_\tau \times \mathbf{u}_j^h, \frac{\beta}{\alpha_j} \nabla_\tau \times \mathbf{e}_i^h \right\rangle_{\mathcal{T}_{ji}} - k_0^3 \left\langle \mathbf{u}_j^h, \frac{\gamma}{\alpha_j} \nabla_\tau \rho_i^h \right\rangle_{\mathcal{T}_{ji}} \end{aligned} \tag{30}$$

$$k_0 \langle \phi_i^h, \rho_i^h \rangle_{\mathcal{T}_{ij}} + \langle \nabla_\tau \phi_i^h, \mathbf{j}_i^h \rangle_{\mathcal{T}_{ij}} = 0 \tag{31}$$

$$k_0 \left\langle \phi_j^h, \rho_j^h \right\rangle_{\mathcal{T}_{ji}} + \langle \nabla_\tau \phi_j^h, \mathbf{j}_j^h \rangle_{\mathcal{T}_{ji}} = 0 \tag{32}$$

$$\sum_N \left\langle \mathbf{w}_i, s_N \frac{\theta_i}{2\pi} \mathbf{j}_N \right\rangle_C = 0 \tag{33}$$

$$\sum_N \left\langle \mathbf{w}_j, s_N \frac{\theta_j}{2\pi} \mathbf{j}_N \right\rangle_C = 0 \tag{34}$$

$\forall (\mathbf{w}_i^h, \mathbf{w}_j^h) \in \mathbf{X}_i^h \times \mathbf{X}_j^h$, $(\mathbf{v}_i^h, \mathbf{v}_j^h) \in \mathbf{Y}_i^h \times \mathbf{Y}_j^h$, and $(\phi_i^h, \phi_j^h) \in Z_i^h \times Z_j^h$.

Note that the corner-edge penalty terms, (33) and (34), are evaluated with each sub-domain, consequently, the new formulation is applicable to both conformal and non-conformal meshes.

Once again, we conducted the eigenvalues analysis of the DD matrix with FOTC and SOTC-Full after inclusion of corner-edge penalty terms (33) and (34). Figs. 9 and 10 give the eigenspectra for conformal and non-conformal meshes, respectively.

Table 1a
Odd numbered corner edges entries in eigenvectors.

	j_1	j_3	j_5	j_7
Zero eigenvalue	(0.202, 0.0192)	(0.202, 0.0192)	(0.202, 0.0192)	(0.202, 0.0192)
Non-zero eigenvalue	(0.213, 0.0805)	(0.190, −0.0817)	(−0.190, 0.0817)	(−0.213, 0.0805)

Table 1b
Even numbered corner edges entries in eigenvectors.

	j_8	j_2	j_4	j_6
Zero eigenvalue	(−0.202, −0.0192)	(−0.202, −0.0192)	(−0.202, −0.0192)	(−0.202, −0.0192)
Non-zero eigenvalue	(−0.213, −0.0805)	(−0.190, 0.0817)	(0.190, −0.0817)	(0.213, −0.0805)

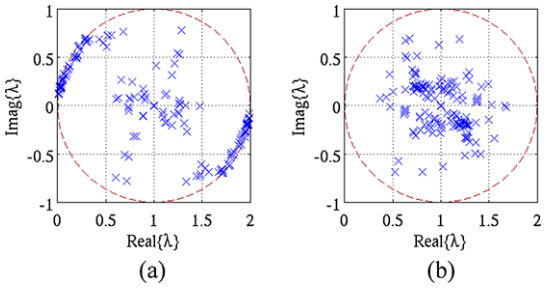

Fig. 9. Eigenspectra of conformal DD for an air box (a) DD with FOTC; (b) DD with SOTC-Full.

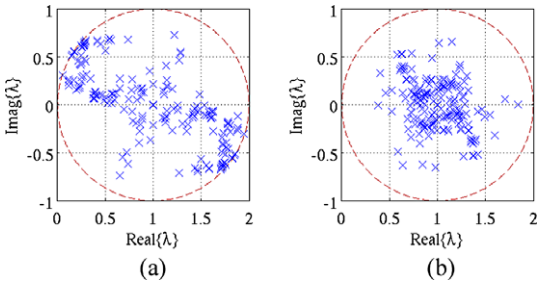

Fig. 10. Eigenspectra of non-conformal DD for an air box (a) DD with FOTC; (b) DD with SOTC-Full.

Clearly, the clustering of singular eigenvalues has been moved from zero to inside the shifted-unit-circle. Fig. 11 shows the iterative solver convergence for non-conformal DD methods after the inclusion of the corner-edge penalty terms. From Fig. 11 we observe significant improvements compared to the performance reported in Fig. 7(b). Moreover, the advantages of using the SOTC-Full against the FOTC are also evident.

3. Numerical experiments

In this section, we study the accuracy and scalability of the proposed DD method with respect to mesh size using a WR-90 rectangular waveguide. Two additional examples, a microstrip photonic band gap structure and a microwave photonic crystal, are analyzed to show the benefits of employing the proposed non-conformal DD with SOTC-Full to solve large electromagnetic problems with practical interests. Throughout our numerical examples, we employed the mixed order Nedelec elements from [16], with order $p = 2$. A relative residual defined as

$$\xi = \frac{\|M^{-1}(Ax - b)\|_2}{\|M^{-1}b\|_2} \tag{35}$$

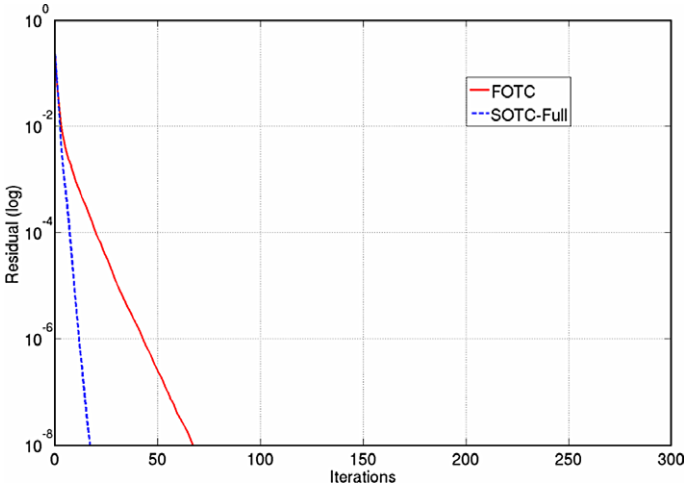

Fig. 11. Iterative solver convergence of DD method (after inclusion of corner-edge penalty).

is used to terminate the DD iterations, with ξ smaller than a specified tolerance. In (35), M is the symmetric Gauss–Seidel preconditioner [12], A is the DD matrix, and b is the excitation vector, and x is the solution at the current iteration.

3.1. Rectangular waveguide

In this example, we study the accuracy and scalability of the proposed non-conformal DD method with SOTC-Full, compared against FOTC, using an X-band (WR-90) rectangular waveguide operated at 10 GHz. The geometry of the waveguide is depicted in Fig. 12(a). Here λ_0 is the wavelength in free space. Both ends of the waveguide are terminated by a first order ABC. The waveguide is partitioned into six sub-domains, as shown in Fig. 12(b). These sub-domains are meshed independently and quasi-uniformly such that the interface meshes do not match. The mesh size is varied from $h = \lambda_0/4$ to $h = \lambda_0/16$ and the GCR (10) solver is used. Fig. 13(b) compares the accuracy of the computed transmission coefficient (S_{21}), using the non-conformal DD method with SOTC-Full against the single-domain vector finite element method. It is seen from the figure, the non-conformal DD with corner-edge penalty terms give almost identical solutions to the conventional FE method. The number of iterations required for DD with FOTC, SOTC-TE and SOTC-Full are given in Fig. 14(a)–(c). We note that the number of iterations significantly reduced by using the SOTC-Full. Furthermore, the proposed SOTC-Full with corner-edge penalty terms is quite insensitive to mesh size because it deals effectively with both TE and TM evanescent modes.

3.2. Microstrip photonic-bandgap (PBG) structure

The second example we use is a microstrip PBG structure. The geometry of the PBG structure is shown in Fig. 15. There are 10 dielectric disks between the microstrip line and the ground plane. The thickness and width w of microstrip are 0.5 mm and 19.625 mm, respectively. The disk spacing is equal to the microstrip width and the disk radius is 3.925 mm with dielectric constant $\varepsilon_r = 9$. The background is simply free space with relative permittivity $\varepsilon_r = 1$. The simulation uses 10 sub-domains. 303,834 DOFs are required for FOTC and SOTC-TE; and 312,985 DOFs are required for SOTC-Full. We study the

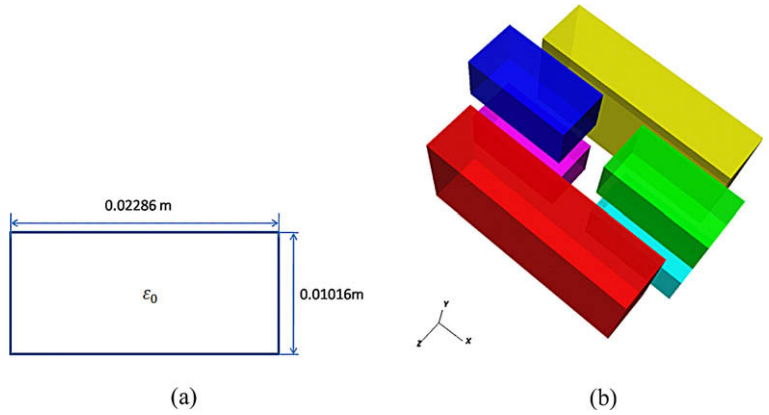

Fig. 12. A WR-90 waveguide (a) cross-section; (b) domain partition.

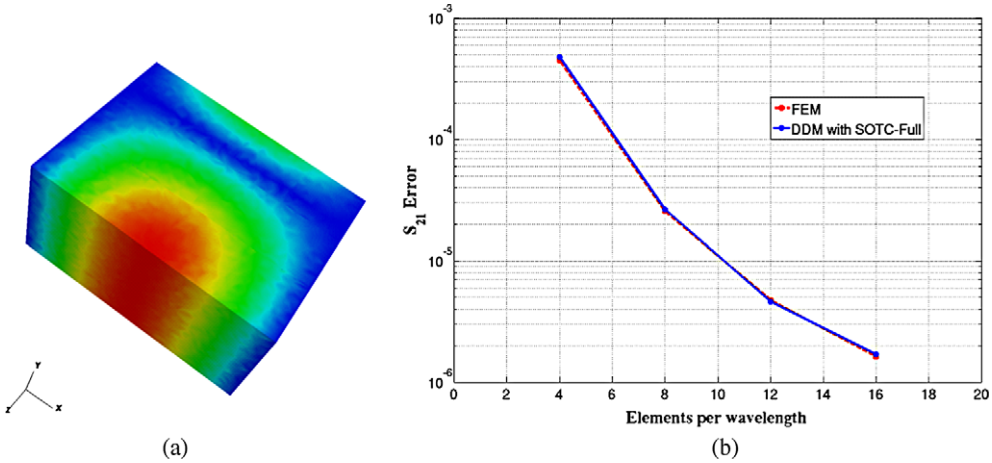

Fig. 13. A WR-90 waveguide (a) the electric fields at 10 GHz; (b) error in transmission coefficient.

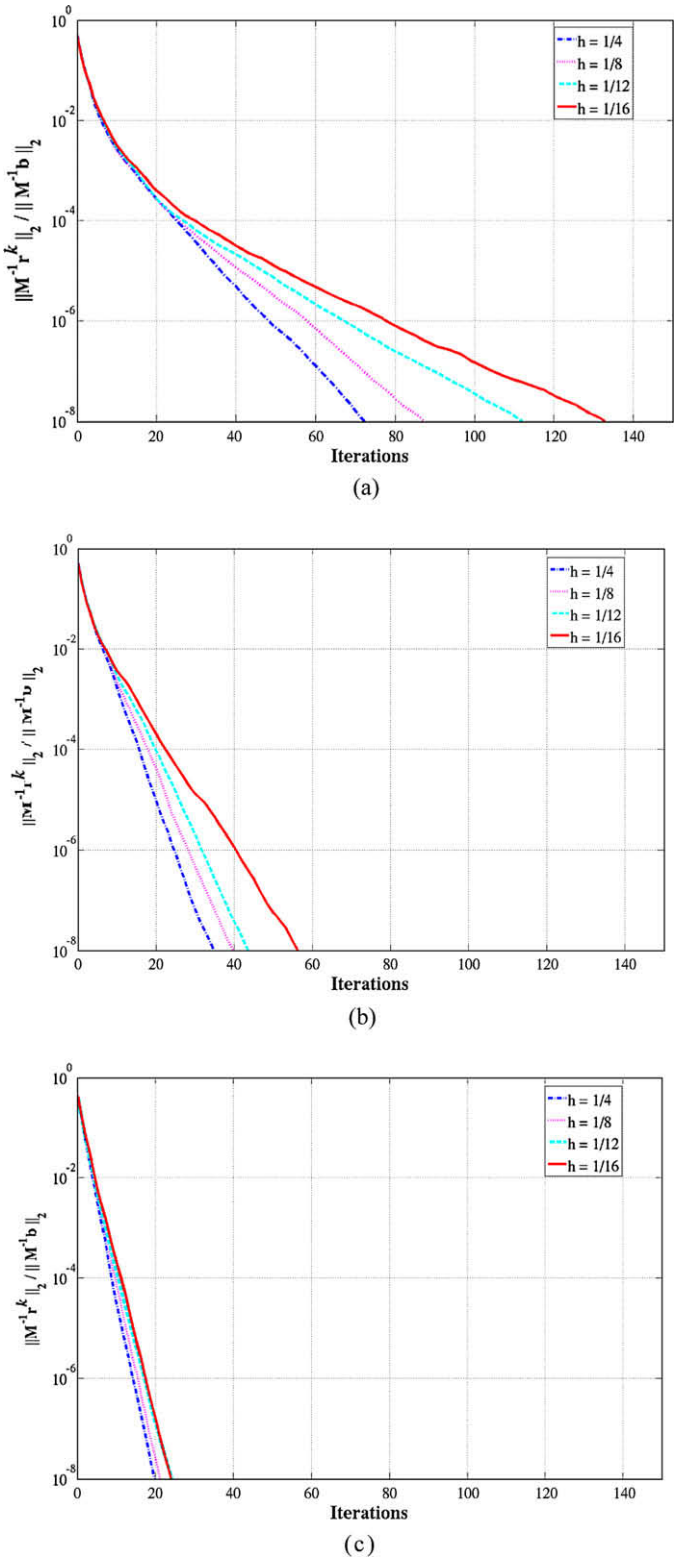

Fig. 14. Iterative solver convergence for a rectangular waveguide with non-conformal domain partition (a) FOTC; (b) SOTC-TE; (c) SOTC-Full.

convergences of DD with FOTC, SOTC-TE and SOTC-Full with stopping criteria of $\xi = 10^{-8}$, as shown in Fig. 16. We see that the SOTC-Full and SOTC-TE converge much faster than the FOTC. This can be attributed to the small mesh elements in the vicin-

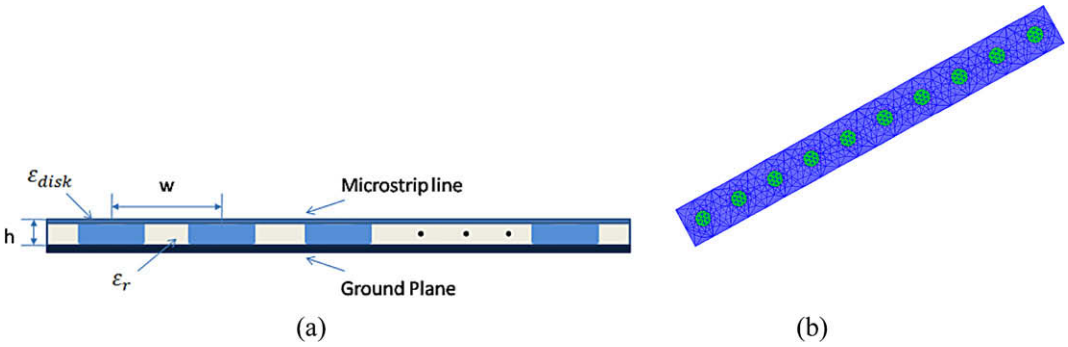

Fig. 15. Geometry of the microstrip PBG structure (a) slide view; (b) top view.

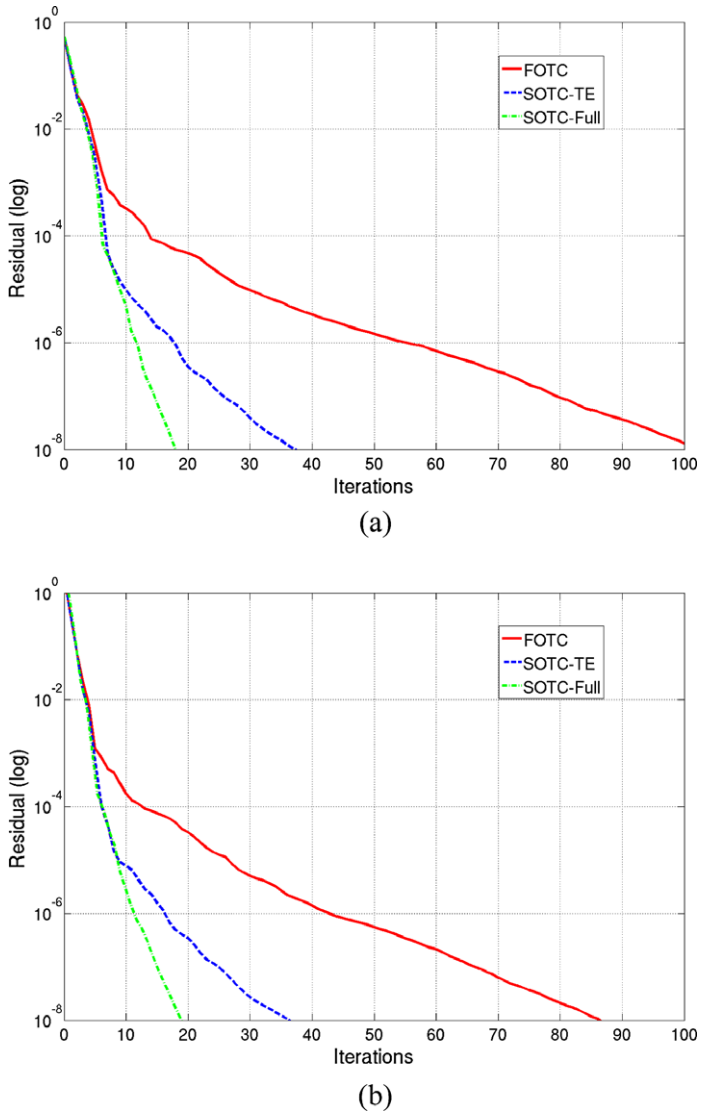

Fig. 16. Solver convergence for PBG structure (a) $f = 3$ GHz; (b) $f = 5$ GHz.

ity of the fine features of the geometry. By moving the TE evanescent eigenvalues away from the origin, the SOTC-TE provides great improvement over FOTC. As SOTC-Full damps both of the TE and TM evanescent modes, it therefore performs even better than the SOTC-TE.

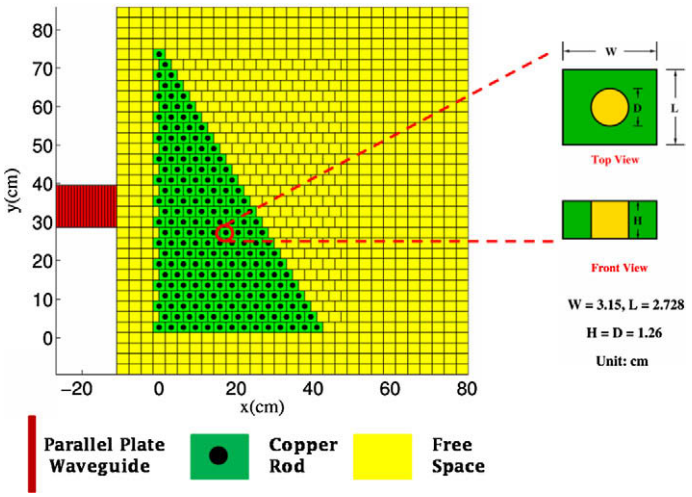

Fig. 17. Geometry and domain partition of the microwave photonic crystal.

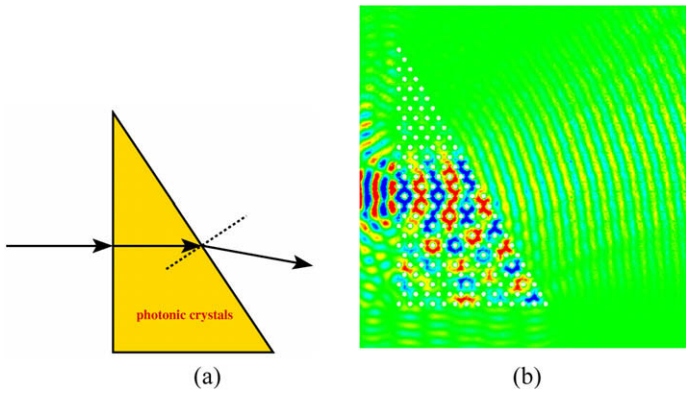

Fig. 18. MPC operated at 6.6 GHz (a) positive reflection; (b) electric field.

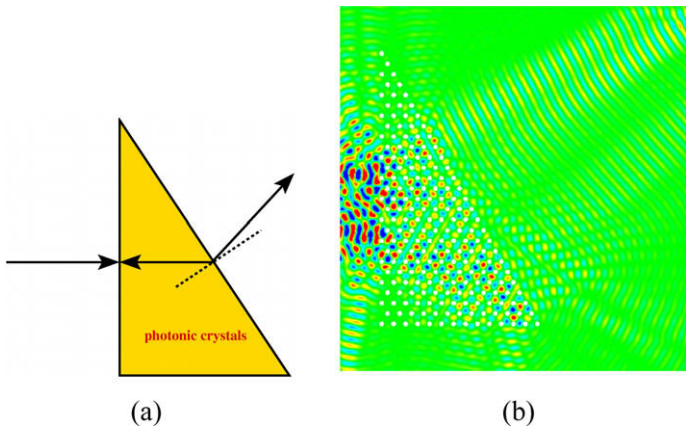

Fig. 19. MPC operated at 9.7 GHz (a) negative reflection; (b) electric field.

3.3. Microwave photonic crystal

To examine the proposed method's performance on practical large-scale problems, a microwave photonic crystal (MPC) [17] is simulated. This MPC includes an array of cylindrical copper rods forming a triangular lattice, and a parallel plate waveguide as excitation. The geometry and domain partition are depicted in Fig. 17. The total computation domain is decomposed into three types of region. They are parallel plate waveguide, copper rod and free space. In this simulation, not only the

Table 2
Computational statistics for MPC simulation, $f = 6.6$ GHz.

Transmission condition	DOFs	Preconditioning time (hh:mm)	Iterations $\xi \leqslant 10^{-2}$	Solution time (hh:mm)	Memory usage (MB)
FOTC	7,367,912	00:34	102	02:41	889
SOTC-Full	7,668,164	00:37	35	00:52	924

Table 3
Computational statistics for MPC simulation, $f = 9.7$ GHz.

Transmission condition	DOFs	Preconditioning time (hh:mm)	Iterations $\xi \leqslant 10^{-2}$	Solution time (hh:mm)	Memory usage (MB)
FOTC	10,726,750	00:43	91	03:01	1279
SOTC-Full	11,038,576	00:45	33	01:12	1352

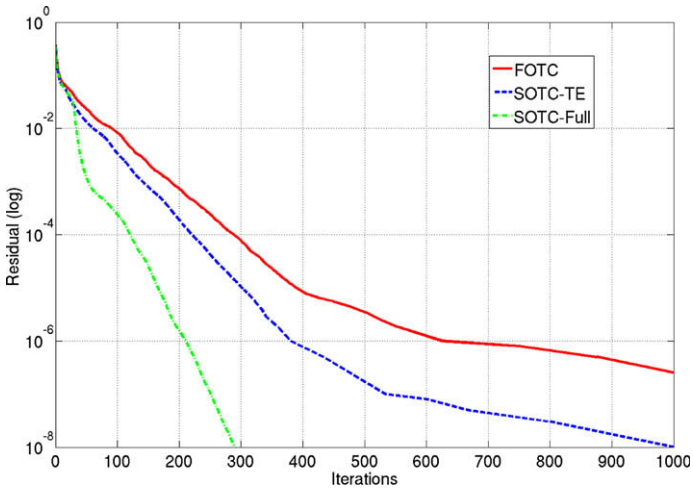

Fig. 20. Iterative solver convergence for a microwave photonic crystal at 9.7 GHz.

meshes on the interfaces are non-matching, but also the adjacent sub-domains are geometrically non-conformal. This example clearly demonstrates the flexibility of non-conformal DD method. Moreover, it illustrates convincingly the superior convergence and robustness of the proposed DD method with SOTC-Full.

The MPC is simulated at 6.6 GHz and 9.7 GHz, respectively, to study the positive and negative refraction indexes phenomenon discussed in [17]. The simulation uses 1048 sub-domains and requires 7,668,164 DOFs at 6.6 GHz and 11,038,576 DOFs at 9.7 GHz. The electric field distributions are given in Figs. 18 and 19. The computational statistics are presented in Tables 2 and 3. The SOTC-Full yields about one-third the iterations as the FOTC. Furthermore, we study the solver convergences of SOTC-Full, SOTC-TE and FOTC with stopping-criteria of 10^{-8}, as shown in Fig. 20. We observe a significant improvement by using SOTC-Full against FOTC.

4. Conclusion

Though the SOTC-TE provides significant improvement over the 1st order Robin TC, it was not complete as it fails to address the convergence of TM evanescent modes. A full second-order transmission condition (SOTC-Full), which accounts for both TE and TM evanescent modes, is developed to improve performance of the non-conformal DD methods. However, it was shown theoretically and experimentally that, to successfully implement and enjoy the full benefits of the SOTC-Full for non-conformal DD methods, we have to suppress problematic singular eigenvalues in the formulation. An implementation with a corner-edge penalty method is proposed and shown to effectively deal with singular eigenvalues by enforcing the divergence free condition. Numerical results verify the analysis and demonstrate the effectiveness of the proposed method on some model problems. Finally, much improved convergence was witnessed using SOTC-Full in conjunction with a corner-edge penalty method for a non-conformal partition of a waveguiding structure and two electrically large problems of practical interests.

Appendix A

The transmission conditions (5) and (6) with (if $\Im(\frac{\beta}{\alpha}) \neq 0$ or $\Re(\frac{\beta}{\alpha}) \geqslant 0$) and ($\Im(\gamma) \neq 0$ or $\Re(\gamma) \leqslant 0$), are equivalent to the boundary conditions (3) and (4).

Proof. Let $\mathbf{j}_1 = \gamma_\tau(\mu_{r1}^{-1}\nabla \times \mathbf{E}_1)$ and $\mathbf{j}_2 = \gamma_\tau(\mu_{r2}^{-1}\nabla \times \mathbf{E}_2)$. Then trivially from (5) and (6), we have

$$\mathbf{j} + \gamma\nabla_\tau\nabla_\tau \cdot \mathbf{j} = 0 \tag{A.1}$$

$$\alpha\mathbf{e} + \beta\nabla_\tau \times \nabla_\tau \times \mathbf{e} = 0 \tag{A.2}$$

on the interface Γ, with $\mathbf{j} = \mathbf{j}_1 + \mathbf{j}_2$ and $\mathbf{e} = \mathbf{e}_1 - \mathbf{e}_2$. Multiplying (A.1) by $\mathbf{j}^*$ and integrating over Γ we obtain, after integration by parts, the real part

$$\langle \mathbf{j}, \mathbf{j}\rangle_\Gamma - \Re(\gamma)\langle \nabla_\tau \cdot \mathbf{j}, \nabla_\tau \cdot \mathbf{j}\rangle_\Gamma = 0 \tag{A.3}$$

and the imaginary part

$$\Im(\gamma)\langle \nabla_\Gamma \cdot \mathbf{j}, \nabla_\Gamma \cdot \mathbf{j}\rangle_\Gamma = 0 \tag{A.4}$$

Obviously, we can conclude that $\mathbf{j} = 0$ on Γ, the required boundary condition, either from $\Re(\gamma) \leqslant 0$ or $\Im(\gamma) \neq 0$.

To prove that (A.2) is equivalent to (3), we first divide (A.2) by α, which is assumed to be non-zero. Multiplying the equation by $\mathbf{e}^*$, integrating over Γ, and performing the usual integration by parts, we have, for the real part

$$\langle \mathbf{e}, \mathbf{e}\rangle_\Gamma + \Re\left(\frac{\beta}{\alpha}\right)\langle \nabla_\tau \times \mathbf{e}, \nabla_\tau \times \mathbf{e}\rangle_\Gamma = 0 \tag{A.5}$$

and for the imaginary part

$$\Im\left(\frac{\beta}{\alpha}\right)\langle \nabla_\tau \times \mathbf{e}, \nabla_\tau \times \mathbf{e}\rangle_\Gamma = 0 \tag{A.6}$$

Once again, with $\Re(\frac{\beta}{\alpha}) \geqslant 0$ or $\Im(\frac{\beta}{\alpha}) \neq 0$, we have (3), namely $\mathbf{e} = 0$ on Γ. □

References

[1] P. Monk, Finite Element Methods for Maxwell's Equations, Numerical Mathematics and Scientific Computation, Oxford University Press, New York, 2003.
[2] B. Després, P. Joly, J.E. Roberts, A domain decomposition method for the harmonic Maxwell equation, in: Iterative Methods in Linear Algebra (Brussels, 1991), North-Holland, Amsterdam, 1992, pp. 475–484.
[3] V. Dolean, M.J. Gander, L. Gerardo-Giorda, Optimized Schwarz methods for Maxwell's equations, SIAM J. Sci. Comput. 31 (3) (2009) 2193–2213.
[4] B. Stupfel, M. Mognot, A domain decomposition method for the vector wave equation, IEEE Trans. Antennas Propag. 48 (5) (2000) 653–660.
[5] V. Rawat, Finite element domain decomposition with second order transmission condition for time harmonic electromagnetic problem, Ph.D. Thesis, The Ohio State University, 2009.
[6] Z. Peng, V. Rawat, J.F. Lee, One way domain decomposition method with second order transmission conditions for solving electromagnetic wave problems, J. Comput. Phys. 229 (4) (2010) 1181–1197.
[7] B. Stupfel, A fast domain decomposition method for the solution of electromagnetic scattering by large objects, IEEE Trans. Antennas Propag. 44 (10) (1996) 1375–1385.
[8] C.T. Wolfe, U. Navsariwala, S.D. Gedney, A parallel finite-element tearing and interconnecting algorithm for solution of the vector wave equation with PML absorbing medium, IEEE Trans. Antennas Propag. 48 (2) (2000) 278–284.
[9] S.-C. Lee, M. Vouvakis, J.F. Lee, A non-overlapping domain decomposition method with non-matching grids for modeling large finite antenna arrays, J. Comput. Phys. 203 (1) (2005) 1–21.
[10] M.N. Vouvakis, Z. Cendes, J.-F. Lee, A FEM domain decomposition method for photonic and electromagnetic band gap structures, IEEE Trans. Antennas Propag. 54 (2) (2006) 721–733.
[11] Y.-J. Li, J.-M. Jin, A new dual-primal domain decomposition approach for finite element simulation of 3-D large-scale electromagnetic problems, IEEE Trans. Antennas Propag. 55 (10) (2007) 2803–2810.
[12] K. Zhao, V. Rawat, S.-C. Lee, J.-F. Lee, A domain decomposition method with nonconformal meshes for finite periodic and semi-periodic structures, IEEE Trans. Antennas Propag. 55 (9) (2007) 2559–2570.
[13] P. Collino, G. Delbue, P. Joly, A. Piacentini, A new interface condition in the on overlapping domain decomposition for the Maxwell's equation, Comput. Methods Appl. Methods Eng. 148 (1997) 195–207.
[14] M.J. Gander, F. Magoulès, F. Nataf, Optimized Schwarz methods without overlap for the Helmholtz equations, SIAM J. Sci. Comput. 24 (1) (2002) 38–60.
[15] A. Alonso-Rodriguez, L. Gerardo-Giorda, New non-overlapping domain decomposition methods for the harmonic Maxwell system, SIAM J. Sci. Comput. 28 (1) (2006) 102–122.
[16] D.-K. Sun, J.-F. Lee, Z. Cendes, Construction of nearly orthogonal Nedelec bases for rapid convergence with multilevel preconditioned solvers, SIAM J. Sci. Comput. 23 (4) (2001) 1053–1076.
[17] P.V. Parimi, W.T. Lu, P. Vodo, J. Sokoloff, J.S. Derov, S. Sridhar, Negative refraction and left-handed electromagnetism in microwave photonic crystals, Phys. Rev. Lett. 92 (12) (2004). pp. 127401-(1-4).